Chapter 8: Structure of craters on the Moon and Earth
Copyrighted by WR. Barnhart, 4/1/2021

Abstract

Three craters on the moon; Aristarchus Crater, Piccolomini Crater, and Mare Orientale; and three recognized craters on earth; Meteor Crater, Sudbury Structure, and Vredefort Dome; are examined to determine their common structures, and to evaluate the current model of ballistic projection and crater floor rebound for crater rim formation. The prominence of straight linears show Concentric Global Ring Structures are a ubiquitous occurrence around known craters and made a prominent contribution to the visible structure and heat input to the lithology. The number of prominence ghost craters shows total compressive energy within the energy envelope pattern in the local lithology; not explosive power, ballistic projection and final rebound of the crater floor; was the primary factor in determining crater form for all sizes of impactors. The concept of astral bodies impacting into a significant heat sink accounts for the proliferation of ghost craters of all sizes and suggest the total number of impactor striking the two bodies may total 1000 – 10,000 times the present count.

Introduction

As early as 1610 Galileo looked through his early telescope at the moon's "protuberances and hollows" (page 8a), "prominences and depressions" (page 9b), and "summits and cavities" (page 10b) and compared them to Earth's valleys and mountains. But, he mentioned a unique feature of the Moon's "cavities", they were "perfectly round and circular, as sharply defined as if marked out with a pair of compasses' (page 12b). While some of the moon's craters are distinctly bowl shaped like Aristarchus and Piccolomini craters (Figure 8.1A & B), others like Mare Orientale (Figure 8.1C) show multiple rings and a very different structure. The generally unrecognized "ghost craters" and linears of valleys and ridges that appear everywhere seem to call for added explanation.
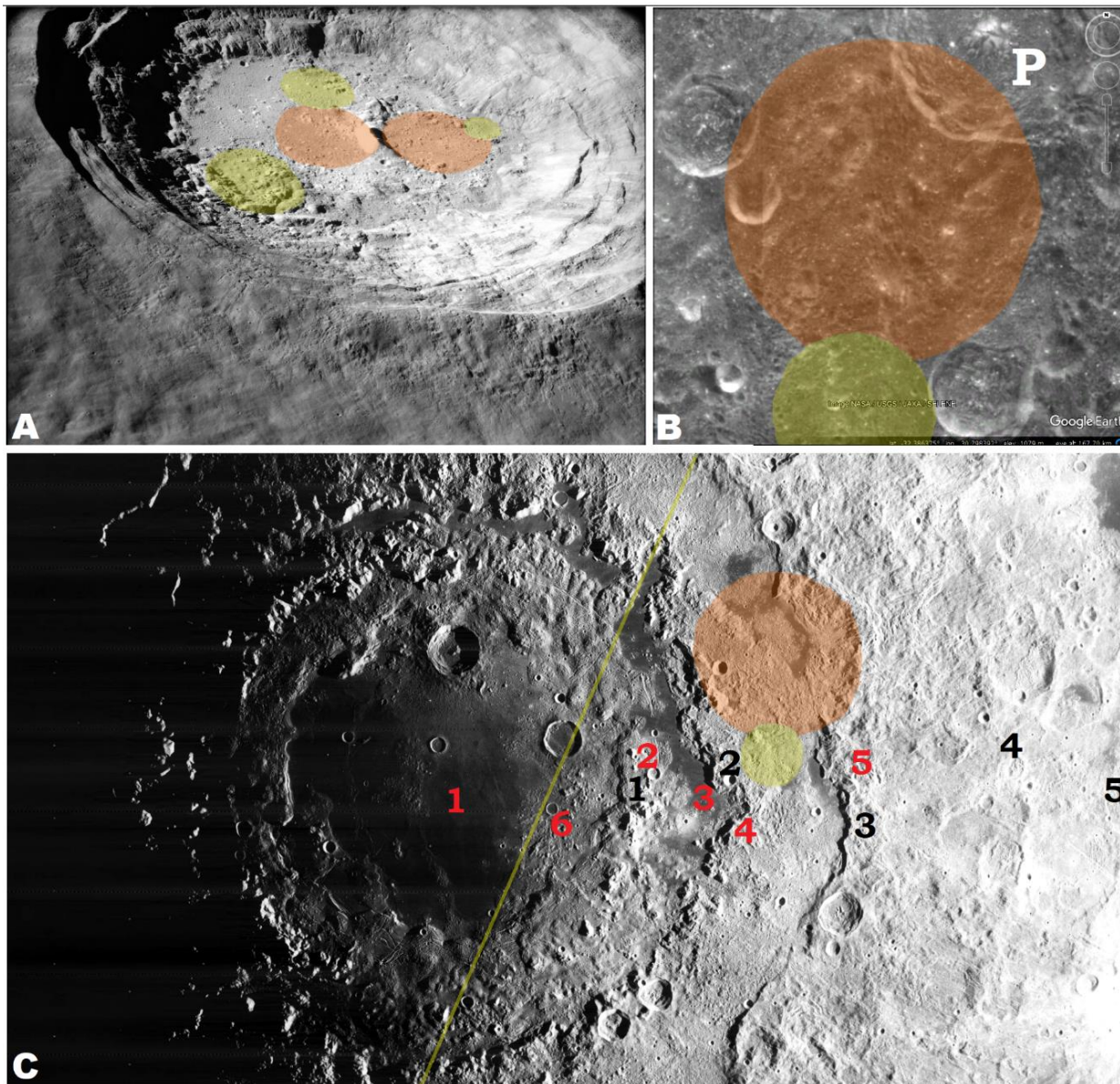

Figure 8.1: Moon Craters. (A) Aristarchus near Mare Imbrium, 40 km diameter. (B) Piccolomini crater (P), 88 km diameter within Mare Nectaris rings, (C) Mare Orientale, 930 km diameter. Representative "ghost craters" indicated in red and yellow circles. How many more ghost craters can you identify? (NASA images)

On earth some craters are bowl shaped, like Meteor crater, Arizona (Figure 8.2A), but others, like Sudbury crater, Ontario (Figure 8.2B), are not nearly as round. When the Vredefort, South Africa is examined (Figure 8.2C), half of it has a distinct round shape, but significant parts of the other half are missing. "Ghost crater" are found around Sudbury and lines in the topography are readily seen in Meteor and Vredefort craters. What are the origin of these regional fractures and what are their connection to the crater's form? The

model for crater formation need to take all of these structures into consideration. Before starting to consider a new model, look at the old model and these six craters and see where they correspond or differ.
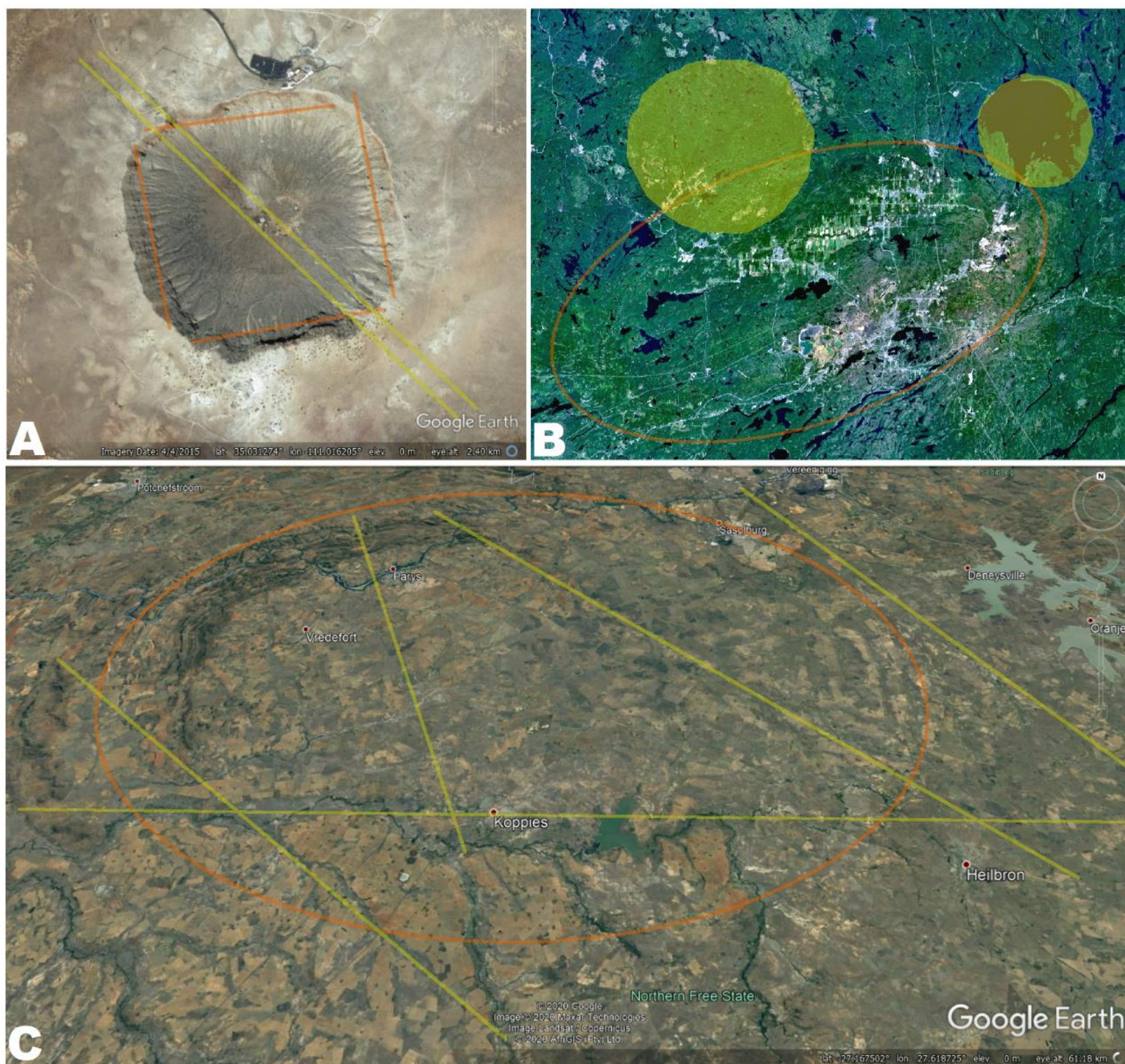

Figure 8.2: Earth craters. (A) Meteor crater, Arizona, U.S.A., <4,000 ft. diameter. (B) Sudbury crater, Ontario, Canada, 130 km long. (C) Oblique view of Vredefort structure, South Africa, 61 km diameter shown. (Images A and C, Google Earth; B, Wikipedia)

The popular model for impact cratering by NASA (Figure 8.3) is largely built on Shoemaker's evaluation of the Meteor Crater (1974) (sometimes called "Barringer" crater, because it is owned by the Barringer family) and his comparison of it to the 1955 nuclear-blast crater, Teapot Ess at the Yucca Flat, Nevada test site. His cratering model divides into two steps. First, the compressional wave moves outward from the penetration site, propelling ejecta radially in ballistic trajectories, while an expanding cavity forms underground. As the cavity breaks the surface a tensional wave continues to expel fragments by expanding gases. The ejection continues until some finite point is reached where the energy available is inadequate to continue projecting material, and here the hinge-joint for overturned strata forms the transient crater rim. The expulsion of ejecta forms a cone-shaped pit with the deepest point at the impactor's penetration site and the limit of excavation forming the rim. Once excavated, the crater is modified by rebound from the compression to form the crater's floor and partial transient rim collapse to form the final rim.

Although Shoemaker does not discuss it, his model has become modified (Figure 8.3) to cover complex craters like Mare Orientale or Mare Nectarous which are believed to have formed their multiple rings by collapse of the transient rim along concentric faults, or some type of liquefaction of the returning eject. Complex jetting and rebound are believed to produce the central peak or ring. The model also supposes that the majority of upward movement forming the rim was ejecta, and only a small part was compressional uplift.
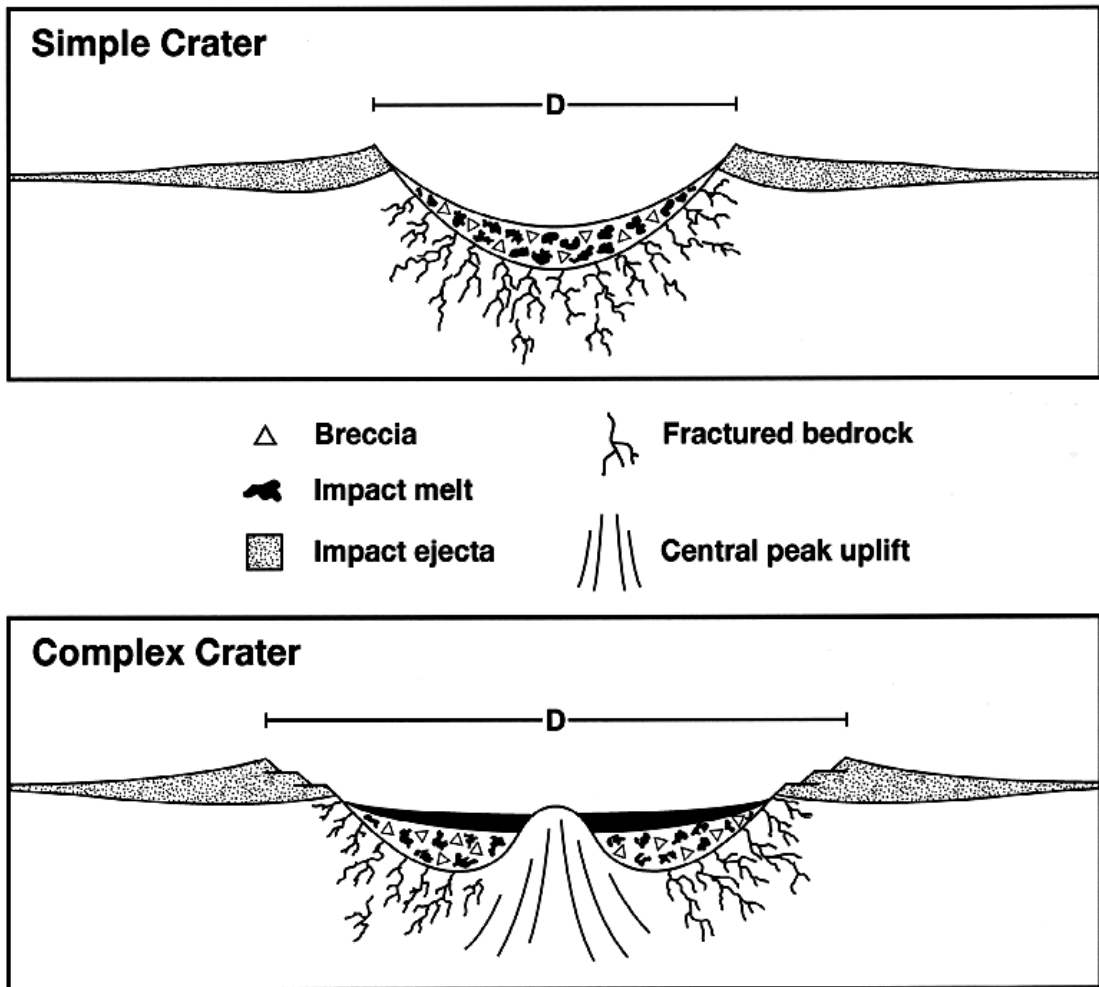

Figure 8.3: Generalized cross section of simple and complex crater formation by NASA

A model which depends on continued ballistic trajectory of ejecta and crater floor and rim collapse to form the crater rings fails to account for linear patterns is the structure of craters like Aristarchus or the patterns of alternated high and low gravity readings around craters like Mare Orientale.

There is a recognized difference in discussing moon craters from the lowlands, which would compare with our ocean depths, with earth craters from the continents, which would compare with the moon's highlands on its farside. These craters were picked for their familiarity and good image availability, but some significant differences between craters chosen on the two rocky bodies are attributed to continental/ocean depth difference.

Aristarchus

Located beyond the rim of Mare Imbrium (Figure 6.4A), Aristarchus, at 40 km diameter, is a bowl shaped depression. Figure 8.4B shows six linears related to three shear centers. While these are visible at this resolution, Figure 8.4C, at greater resolution, shows these three and three more.

What is the effect of these lines? As Concentric Global Ring Structures (CGRS), they each have a compression part and a following expansion portion (Chapters 3-4). Figure 8.4C gives some hint of the variation in albedo intensity in the various portions of the Aristarchus crater's interior, but it is most definitive in the "central peak" seen in Figure 8.4D. I propose the five numbered divisions are the three major albedo regions divided by two fold zones. Mustard et al (2011) does not recognize the fold zone, and only recognized three of these section (3, 4 and 5). They seem to ignore sections 1 and 2. The high albedo section 3, they identify as probably noritic anorthosite. They identify it as definitely feldspar rich, but contains no mafic material, although other authors have recognized a mafic component in its composition. Section 3's identity as noritic contrast sharply with section 2, which gives a strong impression of beads of melted glass based on the smooth cascade down the back side of central peak structure in other views. Sections 1 and 5 may be a breccia layer of noritic with some melt beads giving a different albedo reflection because of the texture. Mustard et al gives no definitive composition differences beyond feldspar, as his bases for the mineralogy of each major divisions. They do mention glass melt would be expected to produce a dark, poor albedo, contribution, and beads of melted glass are found on earth, believed associated with several crater locations. If the shock/compressional wave produced the solid noritic lithology and the release/

expansion wave turned part of it to fine breccia which mixed in the air with droplets of melt, this could produce the gray colors. Successive CGRS expression near to each other would cause the small folding recognized in this central uplift (Figure 8.5).
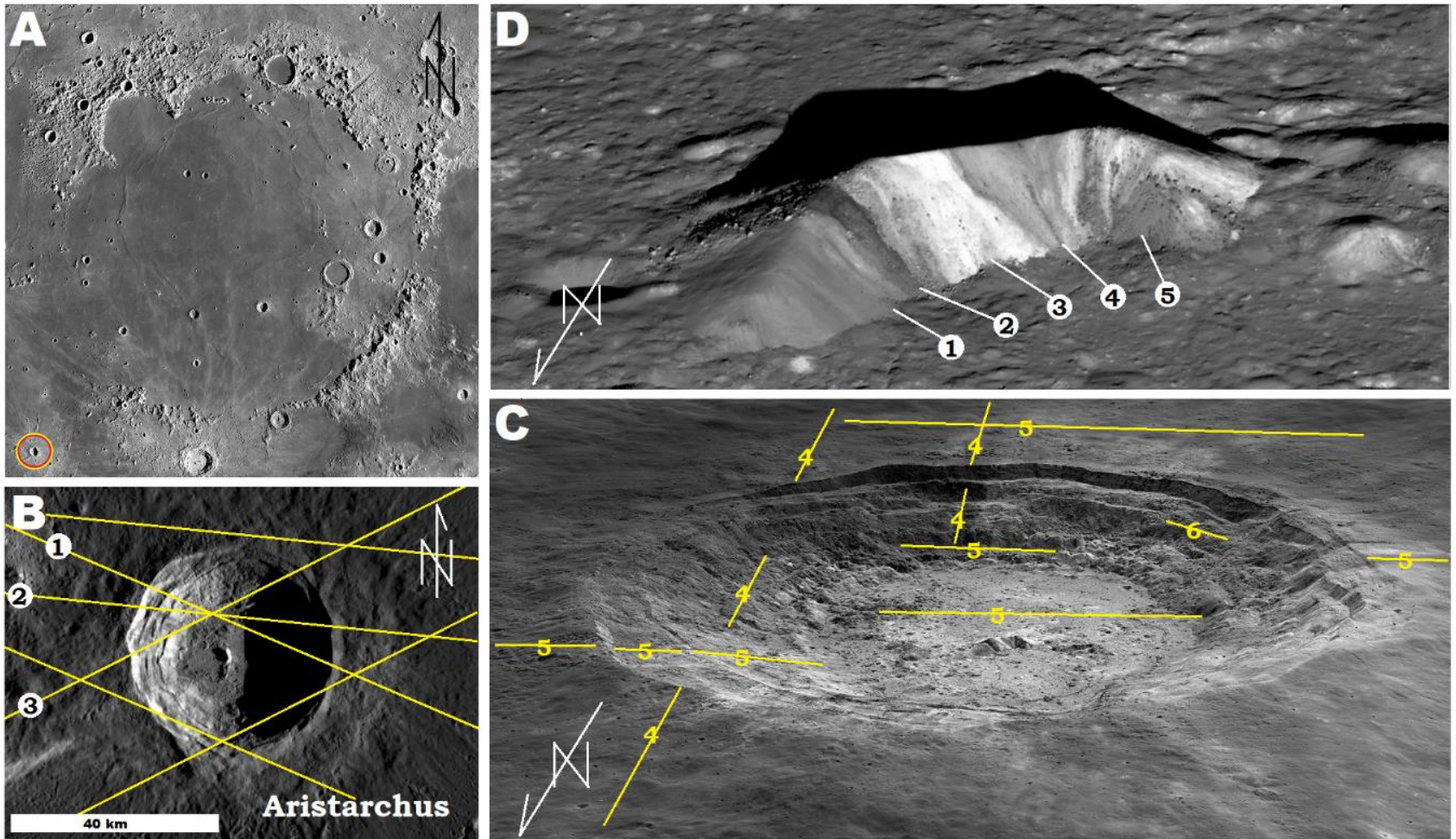

Figure 8.4: Aristarchus crater. (A) Location in relationship to Mare Imbrium. (B) Vertical view with indication of three sets of linears seen in topography view. (C) Oblique view with three additional sets of linears marked. (D) Central Uplift showing divisions. (Image credit: NASA.)
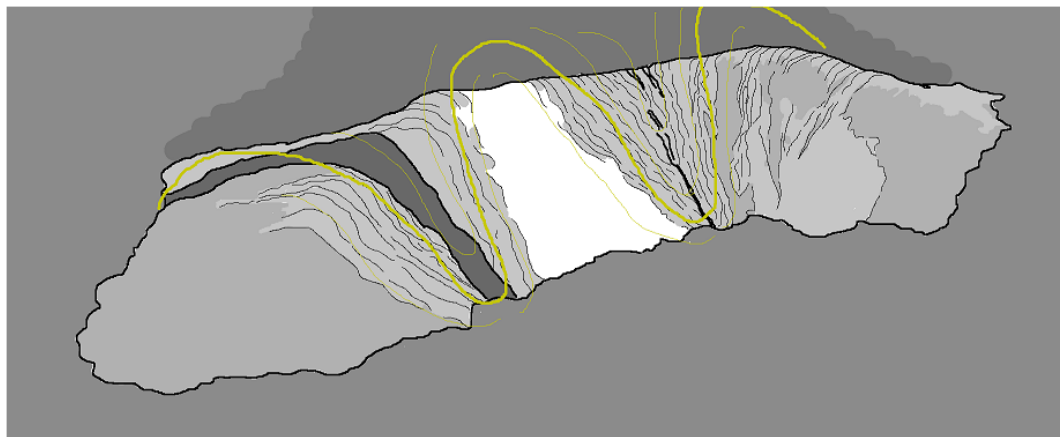

Figure 8.5: Diagram of albedo on central uplift of Aristarchus crater showing folding pattern with closed syncline. See Figure 8.4D for correlated photograph.

Figure 8.6 shows distinct linear orientation to mineral deposits in Aristarchus, whether these linears are running up crater walls, as the pale green, or diagonally across the arc of the crater, as the red. Mustard et al (2011) shows several details from M^3 satellite data from Aristarchus, which all reinforce this perceived linear orientation to its various mineral identifications. If repeated expression of CGRS are delivering patterns of successive expressions of energy, with alternating highs and lows as was seen in the Pacific CGRS in Chapters 3-4, this increased energy would be expected to produce different minerals concurrent with the patterns. Such highly structures patterns denies random ballistic trajectories were involved.
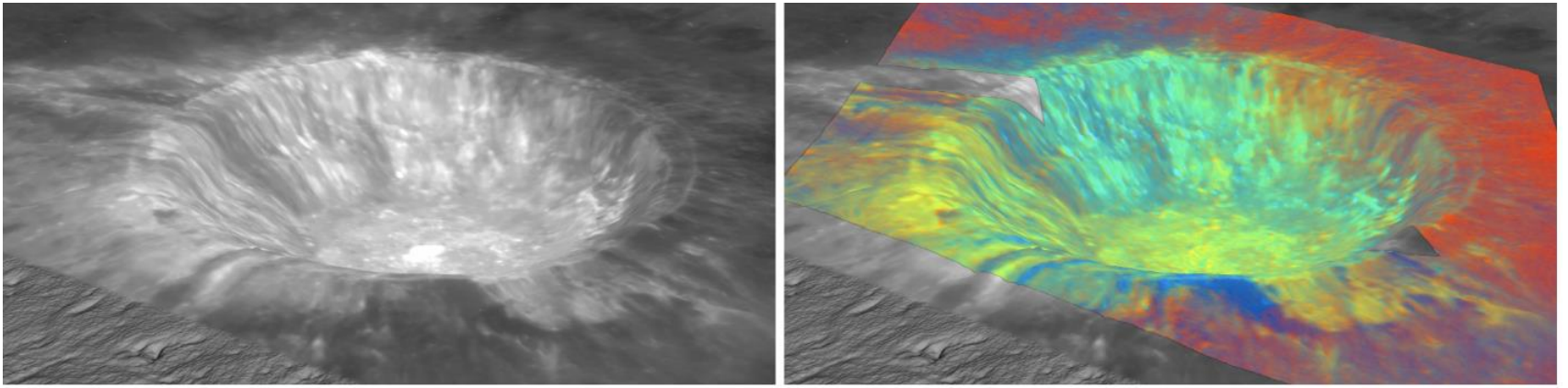
Figure 8.6: Hubble Telescope image of Aristarchus crater comparing visible light (left) and UV spectrum light (right), Specific wave lengths of UV light are believed to identify mineral composition, based on UV spectrum analysis of Meteor Crater, Arizona. (NASA/Goddard Space Flight Center Scientific Visualization Studio, Z.G. Levay (STSci))

In Figure 8.7, besides the six directions of linears, a number of ghost craters can be identified. As none of these cratering events left a significant pit, the rock was at high enough energy that the energy output of the impact was swallowed up in the collision. This is seen in impactor 3 landed both on the flat crater floor and on the slope of the crater wall. It is most identified by the trough left in the release-wave valley. As Mustard et al recognizes that the central peaks are embayed, I suggest it was pushed up as a portion of ghost crater 1 and 2's rims. If both impactors arrived near the same time, the central peak appears to have been squeezed up/lifted by their overlapping compression/shock-waves rings, and pushed out of the center by impactor 2, but stopped by impactor 1.
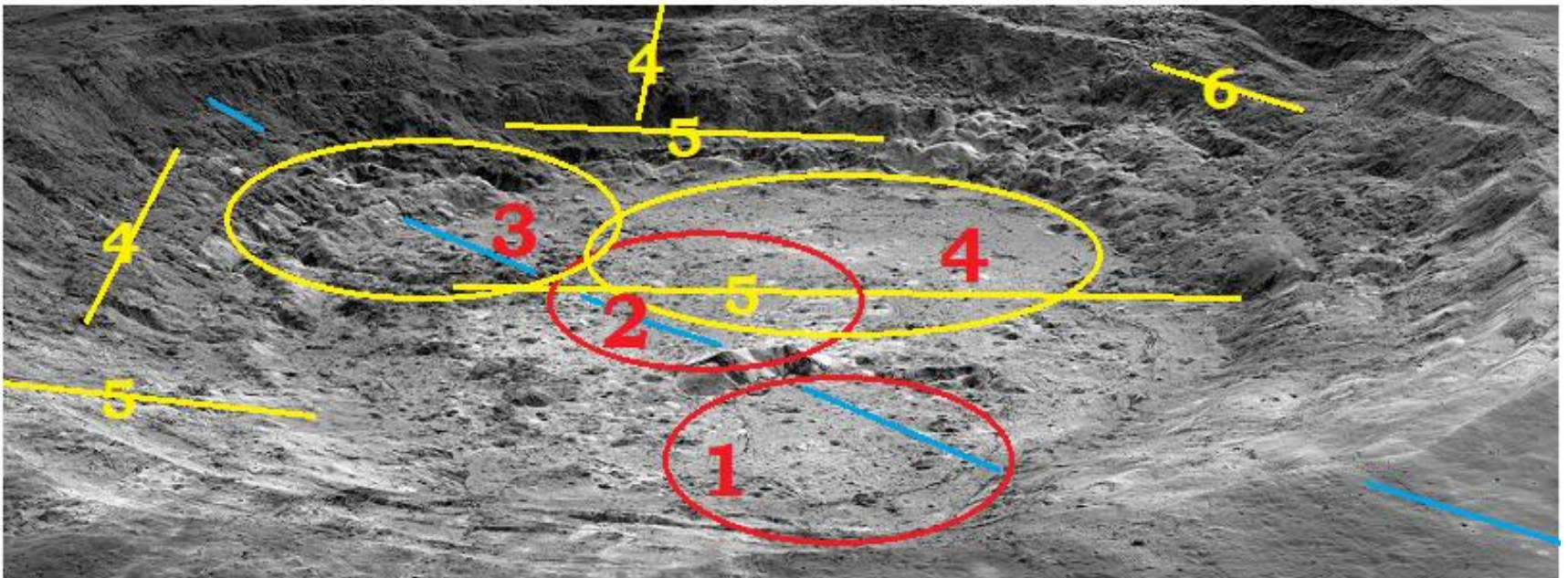

Figure 8.7: Detail of Figure 8.4C showing linears and ghost craters in the floor and walls of Aristarchus crater. Blue linear appears to have been responsible for fold in central uplift, possibly concentric to linear 6, with both forming at similar time to cratering.

Piccolomini Crater and Mare Nectaris

How do we recognizing ghost craters? In Aristarchus crater, Figure 8.7, the most visible indication of a ghost crater is circle 3, where the circle made a distinct trough in the crater wall. This is consistent with the more visible linears left on earth in the Feather River Valley (Chapter 6, Figure 6.11) and Yosemite Valley (Chapter 7, Figure 7.17-18), both in the Sierra Nevada Mountains of California, U.S.A. I proposed these release wave valleys were produced by their respective impactors while the Sierra Nevada Mountain batholith was rising as a result of a CGRS and in a plastic state. This explanation fits the circular trough in circle 3 of Aristarchus crater, also.

Examining Piccolomini crater, Figure 8.8A, eight pairs of circular or arced linears are marked crossing the terraced wall of the crater. The blue sets correspond with the red circle in Figure 8.1B, and include both sides of a release wave valley. These eight pair of linears are extended to full ghost craters in Figure 8.8C, when other topographic clues are included. Compare 8C and 8B to see ghost craters for yourself.

We know Aristarchus crater did not slump because it still show linear lithology consistent with paths that cross the crater. We know Piccolomini crater's rim did not randomly slump because Figure 8.8A shows its configuration is consistent with all three ghost craters that almost certainly formed before it. Additional smaller cratering continued to shape it, Figure 8.9, after it formed.
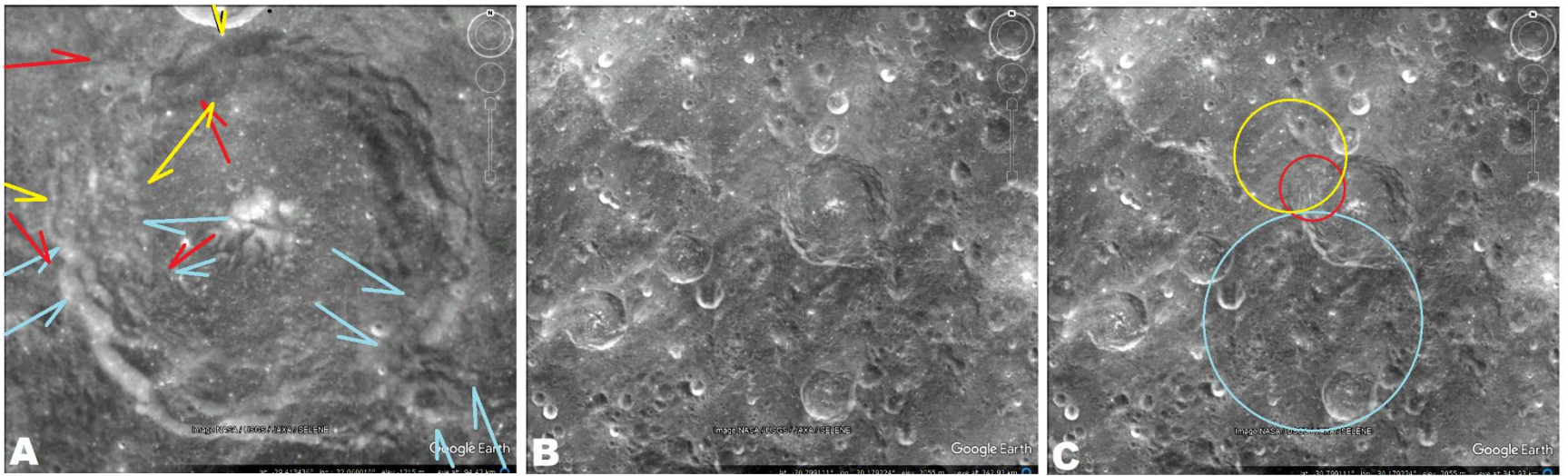
Figure 8.8: Altai Scarp and Piccolomini ghost craters. Compare the two figures, and can the reader recognize the clues for the ghost craters indicated? The blue ring ghost crater was the red solid one in Figure 8.1B. (Image: NASA.)
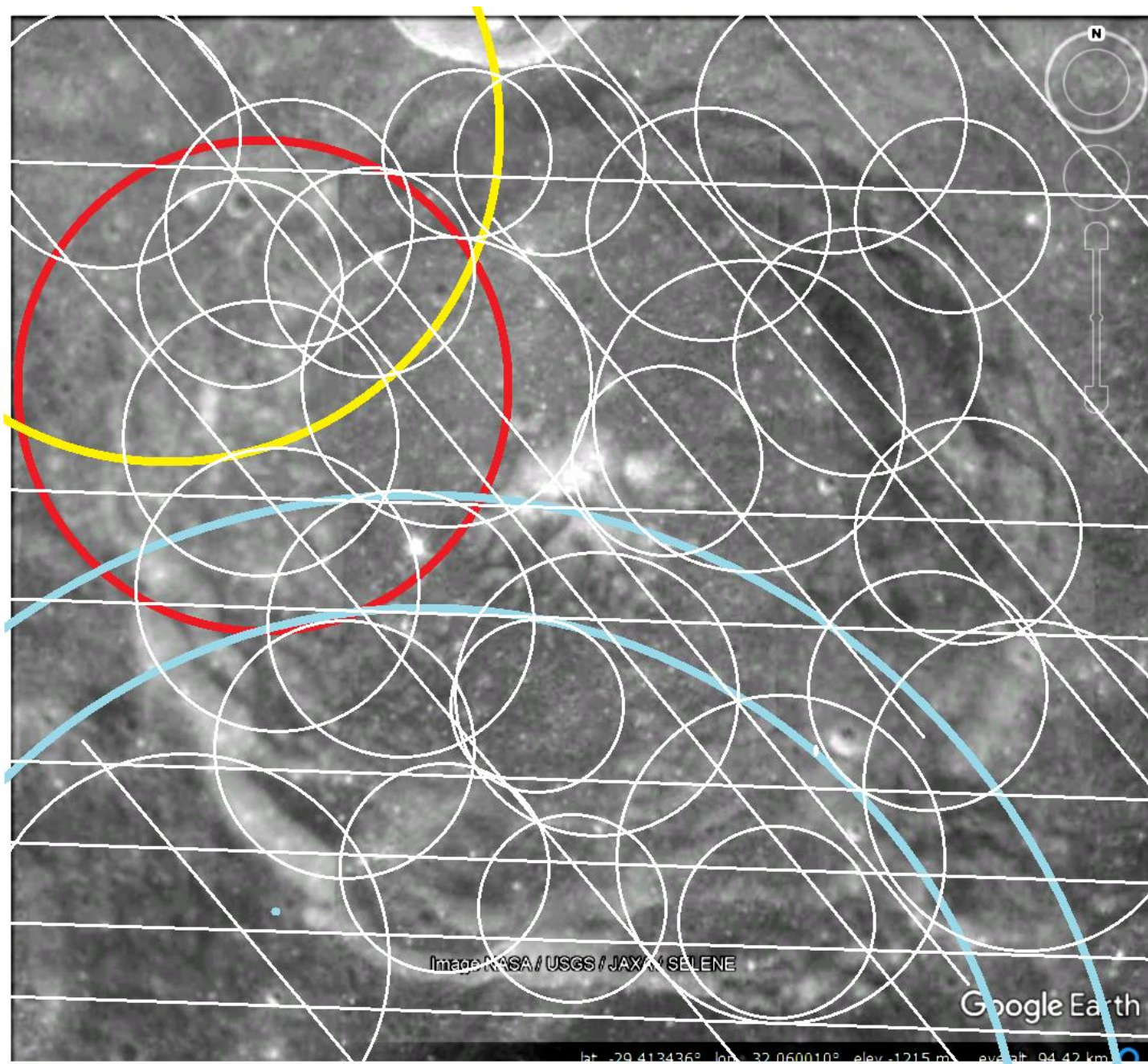

Figure 8.9: Piccolomini crater with the three craters from Figure 8.8, each in its color, and additional straight linears and ghost crater ~7-20 km diameter showing in topography.

Moving outwards from Piccolomini Crater, Figure 8.10 gives an idea of the multitude of ghost craters that can be identified. These are definitely not all of them, but gives an idea of the density at these size ranges.

Were the ghost crater before or after Piccolomini crater? There is no hard and fast reason for this, but I will assume the cratering started at the largest and ended with the smallest. If so, that would mean the ghost craters in Figure 8.10 mostly arrived before the Piccolomini cratering event, and the smaller ones in Figure 8.9 impacted after Piccolomini had been formed. This is certainly the case with Figure 8.9, the blue one. It is larger than Piccolomini, and I propose the release wave valley between the two blue lines seems overly rounded, and I would propose its energy signature was already in the substrate when Piccolomini crater was formed
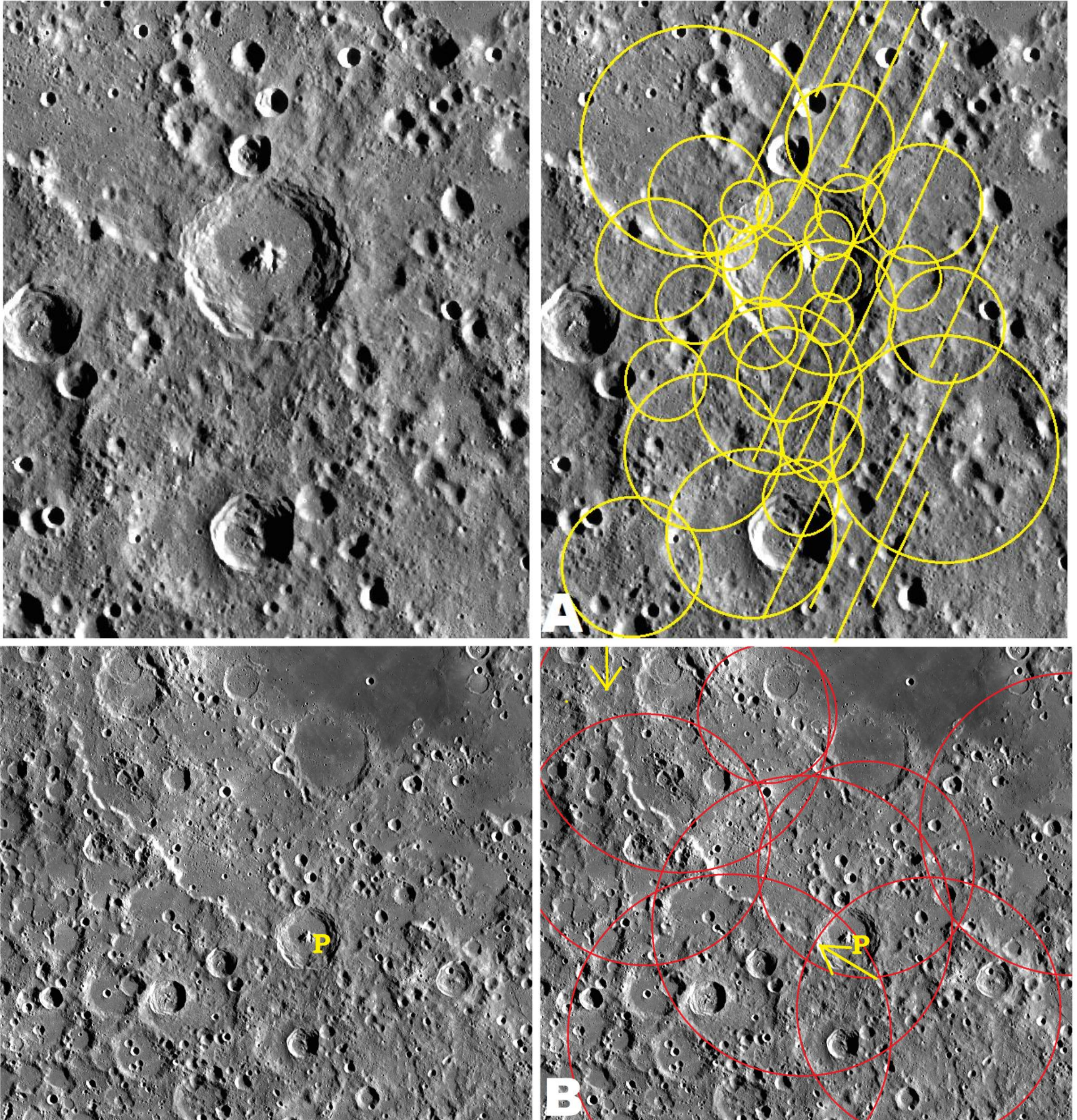

Figure 8.10: (A) Piccolomini crater and some of the ghost craters around it from ~30-180 km diameter. (B) The southwest quadrant of Mare Nectaris, Piccolomini crater (P) and the Altai Scarp (between yellow arrows) showing some of the larger ghost craters in the ~300 – 500 km diameter range. Unmarked image provided for reader to locate ghost circles and linears. (Image NASA)

Hartmann and Kuiper (1962) recognized three rings around Mare Nectaris: Inner ring 400 km diameter, Catharina ring (weak) 600 km diameter, Altai Scarp ring at 840 km diameter. For various reasons, discussed in Chapter 12, I consider the Altai Scarp ring the Original Crater Rim (OCR), so this was a fairly large crater. If my appraisal of linears in the area is correct, Figure 8.10, there are many additional 300-500 km diameter crater rims. Did all of these blast holes in the Mare Nectaris rings, and if not, why not?

When a pebble is thrown into a lake, it does cause a significant splash. That splash is related to its size, speed and angle of entry. But, if that single pebble is followed by a continuing shower of pebbles, the splash with each becomes less and the turbulence of the water is increased. Turbulence is a form of energy, the same as heat, and at the molecular level heat causes a more random movement of molecules to create molecular turbulence.

Impactors arrived at the moon's surface with a great amount of energy contained in its mass and traveling speed. The first impactor makes a significant splash, and transfers its energy into the crust. This original impactor, when it strikes the crust produces a shock-wave that moves outward transferring its energy, which will be ultimately converted to heat energy in the crust. If this impactor is followed by more impactors before the heat has dissipated, the succession of impacts would continue to heat the crust in that area. Eventually, additional impactors would slip into the turbulent crustal surface only adding to the turbulence with shallower ring structure reflecting the energy signature of the shock and release wave. Ghost craters are a result of these impactors cratering into the already heated crust.

Figures 8.9 and 8.10 shows a series of crater sizes from 7 km to 500 km diameter. While all smaller craters may not have formed after the larger ones, it would make sense that many smaller craters occurred after the larger craters to make them still visible.

The recognition of ghost craters is critically important in understanding cratering. The standard explanation is that ghost craters typically occur earlier than more distinct craters, and the ghost craters were partially obscured by ejecta from the later impacts. Figures 8.7 and 8.9 show evidence for ghost craters is contained in the crater rim. The visual indication is not that the ghost craters have become obscured, but they never formed the topographic relief that the more pronounced Piccolomini and Aristarchus craters did. Why are some craters more visible?

Observations: Mare Orientale

Looking at the combined topography and gravity color map overlay of Mare Orientale, Figure 8.11, gravity highs do largely correspond to topographic highs. This would mean that the topographic highs (crater rings 2, 4 and 5) were not just loose ejecta thrown up on the surface by ballistic trajectory as the NASA model suggest (Figure 8.3). Ring 3, between highs 2 and 4, is the lowest gravity reading on the figure, and it follows directly after the high, not slowly grades into it and is followed by another gravity high.

Figure 8.11A shows the higher gravity reading extends to spot 6 where a distinct straight linear (a CGRS, Chapters 3-5) crosses the center and inner ring 2 and is associated with a higher gravity pattern. This high gravity linear is traced across the entire center of this crater (area 1), where it is referred to as a Mascon (mass concentration, Chapter 10). Figure 8.11B also shows the circle between crater rings 4 and 5, designates a ghost crater, which had to arrive after Mare Orientale and was part of a dense shower of smaller impacyors forming ghost craters (Figure 8.12B) that now cover the entire area. While the ghost crater in Figure 8.11B displaced the topography of both rings 4 and 5, it did not leave a significant record in the gravity pattern.
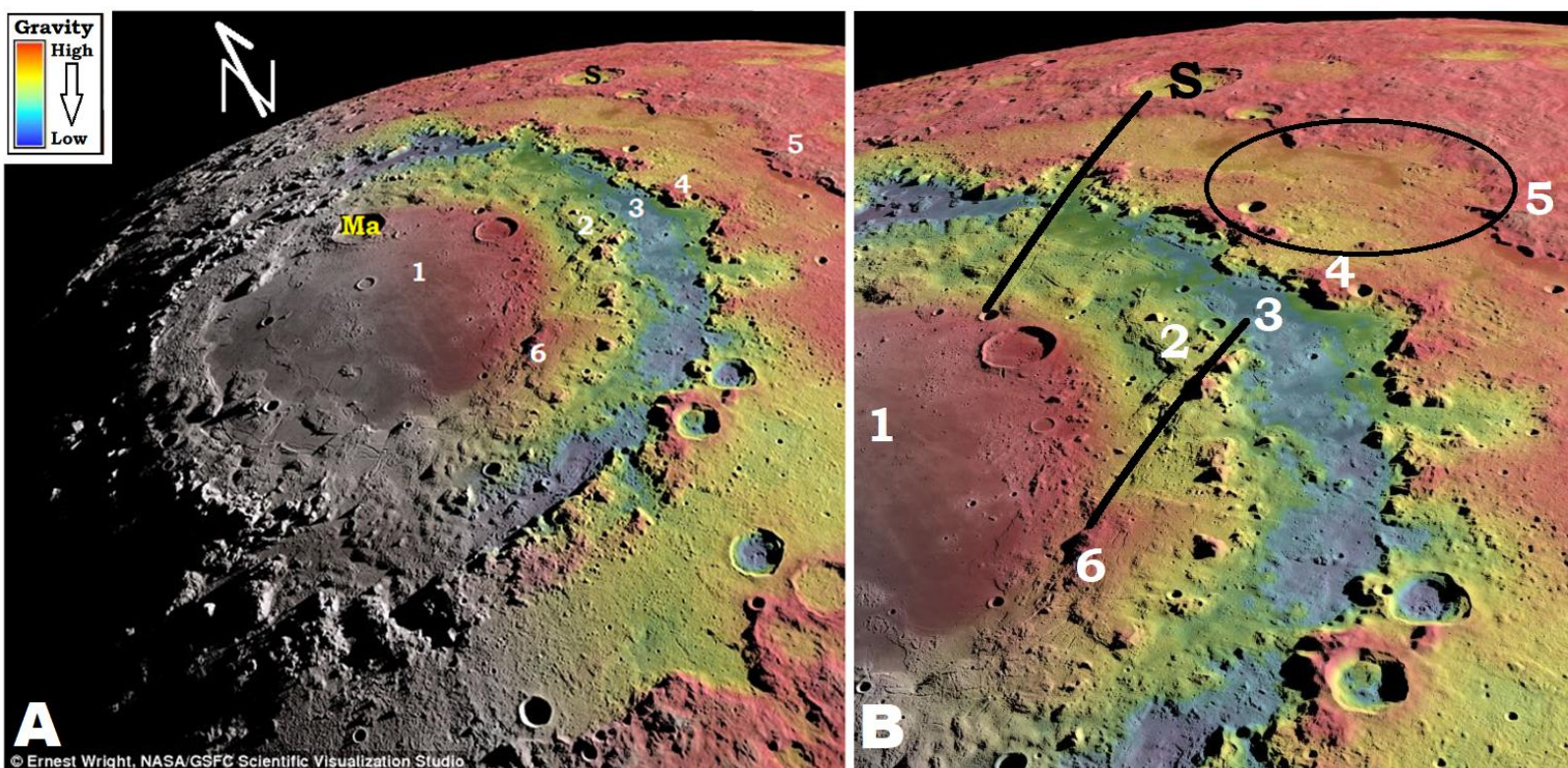

Figure 8.11: Mare Orientale with GRAIL gravity data overlaid on LRO topography data. M= Maunder, S= Schlüter

Mare Orientale is known for its many "radial" valleys, but it is seen (Figure 8.12A) that some of the linears are straight and some are arched, and most are not truly radial. Many of them form pairs of parallel lines, about 20-40 km apart, with a valley in between. This width recalls the Pacific Fracture Zones (Chapters 3-4), where the release valley followed the high scarp of the shock wave. Arced linears would be closer annulus to stress centers and straight linears would be small circle expression of more distant stress centers. They are all CGRS, commonly referred to as regional fracture zones and not radial fractures. Those that were previous to the Orientale cratering event, opened up in the cratering process and vented ejecta, but many others were after the impact and added their energy/heat to the cumulative total in the crust around the crater, that was already made plastic from the impact and released mantle heat.
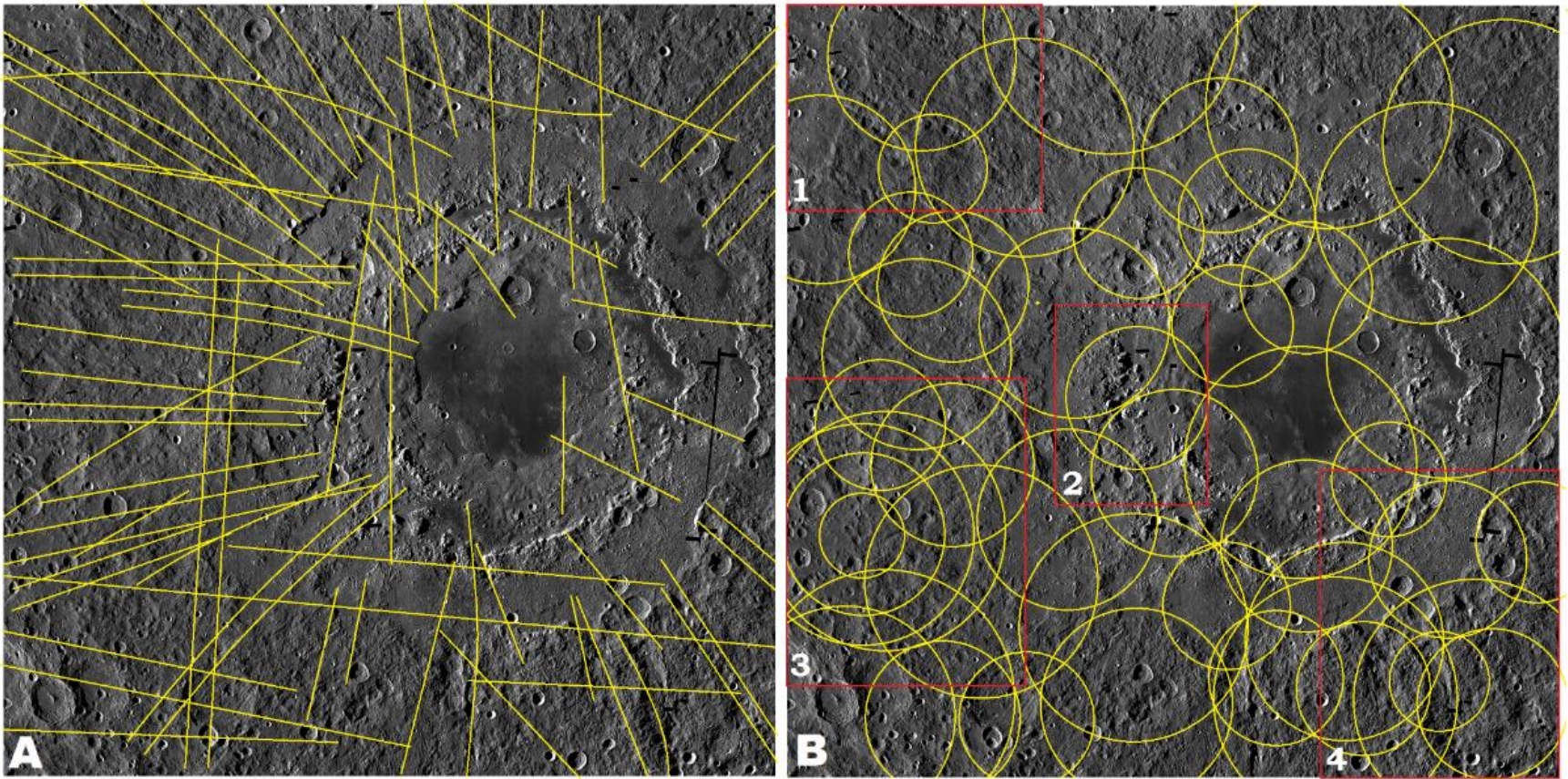

Figure 8.12: Mare Orientale showing some of the (A) straight and arced and (B) circular lineaments seen at this resolution. Red rectangles are location of details in Figure 8.6. Circular Lineaments between 200-400 km diameters. (Image modified from NASA/LROC/WAC March 12, 2011.)

Location of visible craters

Recognizing the numbers of ghost craters, why are these smaller craters more visible in some areas than others? Comparing smaller areas of Figure 8.13 shows many craters are located where circles overlap other circles or where linears CGRS overlap with circles.

Figure 8.13.1A & B. Arrow 1 points to the clues for ghost crater 4. It is not really a ridge or a valley, but a series of disruptions in those tight linears and valleys, now dark with possibly lava flows. This visibility is similar to how CGRS were seen in the topography of California, in Chapters 6-7. In Figure 8.6.1A, between linears, 2 and 3, is darker from the small craters they contain, and 2 has more visible craters than 3. There has to be some reason for this. When ghost crater 5 is drawn its linear divides the craters in 3. Figure 8.6.1B shows the craters just inside ghost crater 5 are divided by the linear from another ghost crater.

In Figure 8.13.2A, linear 1 is primarily in the dark area, between protrusions across the dark (lava?). By contrast linear 2 is defined by a series of small craters. Based on Figure 8.12B, the ghost craters carpet the surface possibly in several layers, and it is a logical conclusion to assume the small craters likewise carpet the entire area. This means when we can see only a few, there is some reason that these few are visible. Because the more visible craters correlate with the linear patterns, it is reasonable to conclude something in the straight and circular linears makes them more or less likely to be visible. I correlate it with the alternating expression of the shock and release waves. Dark spots 3, 4 and 5 are quite round and suggest craters, why would some ghost craters show up as light rings and some as series of dark puddles? Ghost crater 6 gives a clue in its northern region, a dark areas follows the yellow linear just inside it. I propose this is a circular release valley, and dark spot 5 falls within it. Impactors striking within the release valley will leave a darker hole, while craters impacting in the shock ring are more likely to leave a light/visible crater rim.
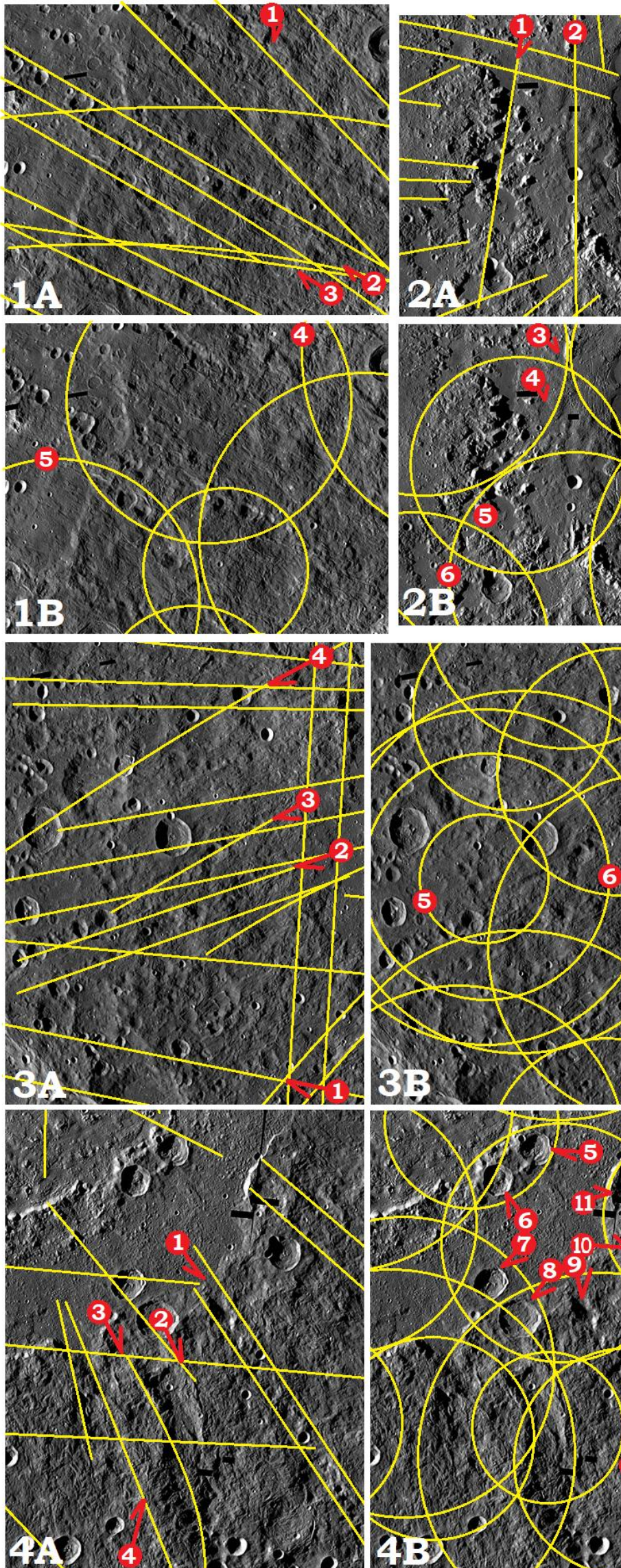
In Figure 8.13.3A, linears 1 and 4 follow a row of small craters in a darker area, while linears 2 and 3 follow a light area linear. Linears 3 and 4 are parallel, so come from the same shear center. I propose their difference again is the shock (Linear 3) and release (Linear 4) waves of the CGRS. Figure 8.13.3B shows stacked craters. Rings 5, 6 and 7 are all from the same impact/ shear centers. These three rings would represent the inner ring (5), OCR ring (6) and second crater ring (7). While ring 8 is nearly concentric, it gives an impression of the confusion that would result trying to draw all rings of every ghost crater. Based on the ambient light bands in Aristarchus central uplift, it is reasonable to assume the color differences reflect different lithology in each area.

In Figure 13.4A, line 1 of craters is between linears, while Linears 2 and 4 have no craters associated with them. Arced Linear 3 again appears in a dark area made up of two arcs, showing it is associated with two ghost craters (Figure 13.4B, crater 12 and one to the west of it). Craters 5-11 occur within the area where multiple craters overlap, and each contributed their energy pattern. These seven craters are not unique in their landing locations, but as a part of the blanket of craters, they were the ones that landed in this uniquely prepared location.

Figure 8.13: Detail areas from Figure 8.5, around Mare Orientale showing relationship between straight linears, ghost craters and expressed craters.

Looking at the northeast quadrant of Figure 8.12, Figure 8.14B shows some of the ghost craters seen at this resolution. Comparing it with Figure 8.12C, the reader can see the topographic clues for the ghost craters. While the ghost craters are most obvious in the darker release wave valleys, beyond the scarp of the rings, many can be seen crossing the scarp. In the specific area of the red ghost crater from Figures 8.1 & 8.4, multiple layers of ghost craters can be seen.
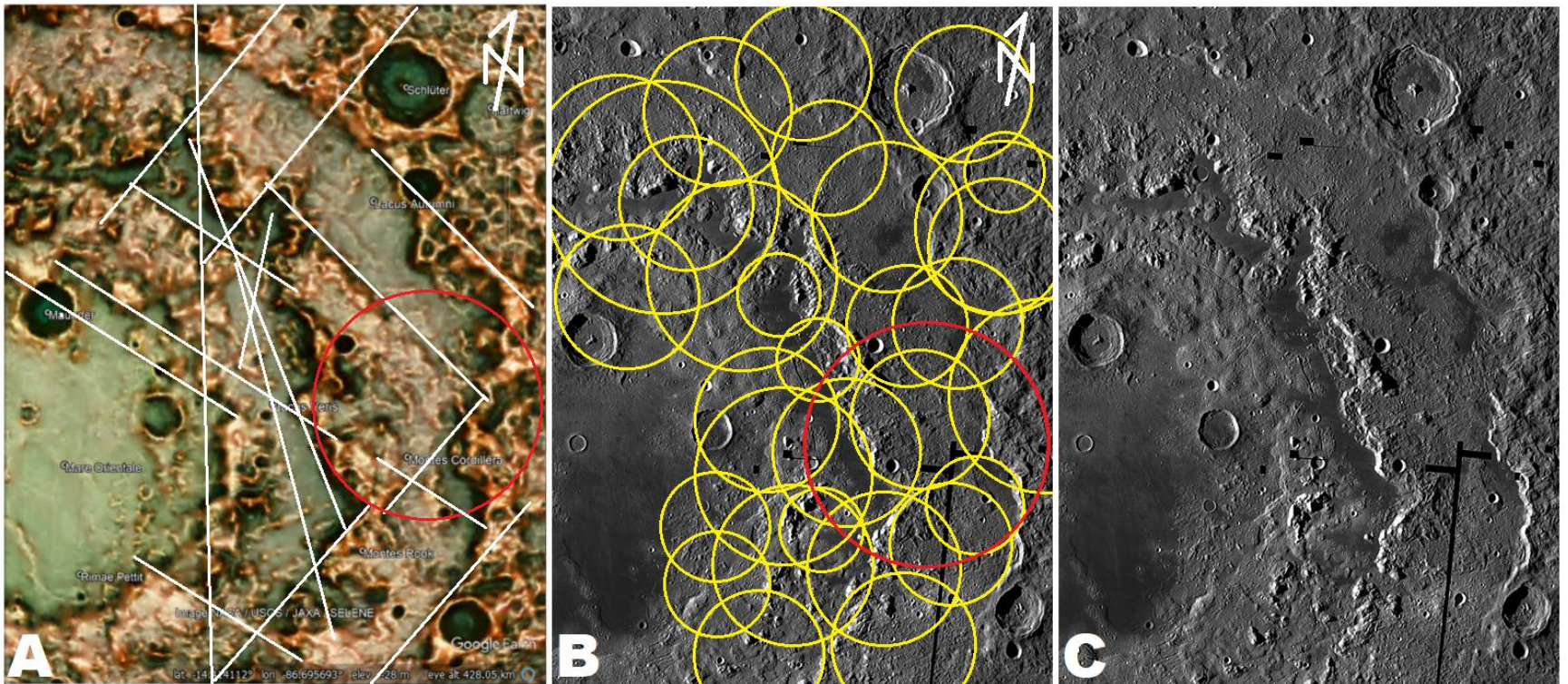

Figure 8.14: (A) Red Relief map of Northeast quadrant of Mare Orientale. Linears in area from CGRS. Red ring, ghost crater from Figure 4. (B) NASA mosaic of same area slightly scrunched from oblique view. Some of the ghost craters sketched. (C) Same view to see indications for ghost craters. Between ~70-200 km diameter. (Image credit: (A) Chiba 2019. (B & C) NASA.)

Hartmann and Kuiper (1962) recognized 5 rings for Mare Orientale; Inner Ring at 320 km diameter, 2nd ring at 480 km diameter, 3rd ring 620 km diameter, Eichstadt ring 930 km diameter, Rocca ring at 1300 km diameter. Using Red Relief (Chiba 2019) (Figure 8.15A), a mapping algorithm that uses black and white shading with red color to accentuate changes in elevation, these five rings were mapped. They correspond with rings 1, 2, 3, 5, and 9. Then additional linears of ridges and gullies were mapped at roughly 75 km wave-lengths. The rings were then transferred to Google Earth's albedo image of the moon's surface (Figure 8.15B) and additional concentric linears can be seen showing it is not the specific location of the individual ring that is important, but the concentric linear to the stress center (Chapter 4). Linears for additional CGRS can be seen between and beyond the rings in Figure 8.15B which extend concentric linears across Mare Nubium to Rupes Recta at 2400 km (-21.97ºN, -7.55ºE) from Mare Orientale's center (with a diameter almost ½ of the moon's circumference).
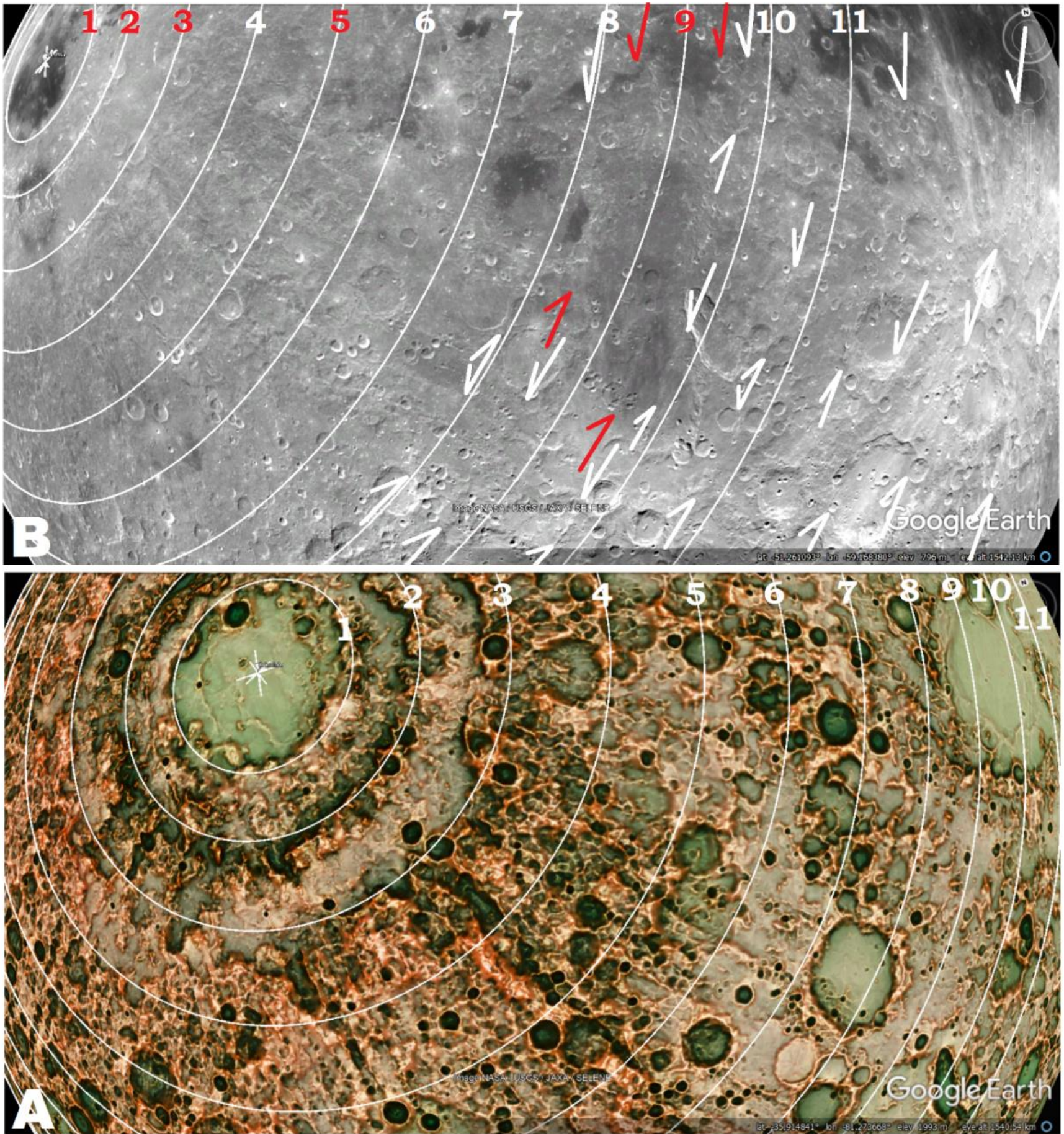
Figure 8.15: Mare Orientale showing CGRS to the center. (A) Red Relief map and (B) Google Earth's Moon Overlay. A ~75 km wave length was chosen for the additional rings. Looking at details on red relief map, how successful was the wave length used?

Now that we have analyzed some moon craters, let us do the same for some earth craters to see if we find similar structures.

Meteor Crater

Meteor [Barringer] Crater in Arizona, U.S.A. is where Shoemaker formulated his model for crater formation. Instead of being a round bowl shape, Meteor crater is noted for its square shape which Shoemaker (1974) attributed to regional fault systems. Figure 8.16 maps four reginal faults found in the area, and connects them to their stress center. The Baldy center (1) is the only close center at 33.90ºN, -

109.56ºE. From the eastern Atlantic, the Verde center (2) at 16.35ºN, -24.12ºE. From just west of Mexico, the Aguj de Anahuac center (3) at 21.03ºN, -106.45ºE. From the northern Atlantic, in the Irminger Sea, the Irminger center (4) at 60.27ºN, -36.44ºE.

CGRS from the Verde and Aguj de Anahuac centers determined the shape of the crater. Significant portions of the Verde CGRS (Figure 8.17 B & C) show as scissor faults (Shoemaker 1974) in the west and east rims of the crater. The north and south sides and the ridges and gullies below the faults on the west and east sides have a major orientation to the Aguj de Anahuac, similarly to ridges and gullies and other CGRS across California (Chapters 6 & 7). The Irminger CGRS is extremely obvious in both topography and gravity image of Figure 8.16, and might be associated with the northeast and southwest corners of the rounded square shape. The fourth regional fault system centered on the more local Baldy center, 180 km radius, and it correlates with the linears of ejecta around the crater.
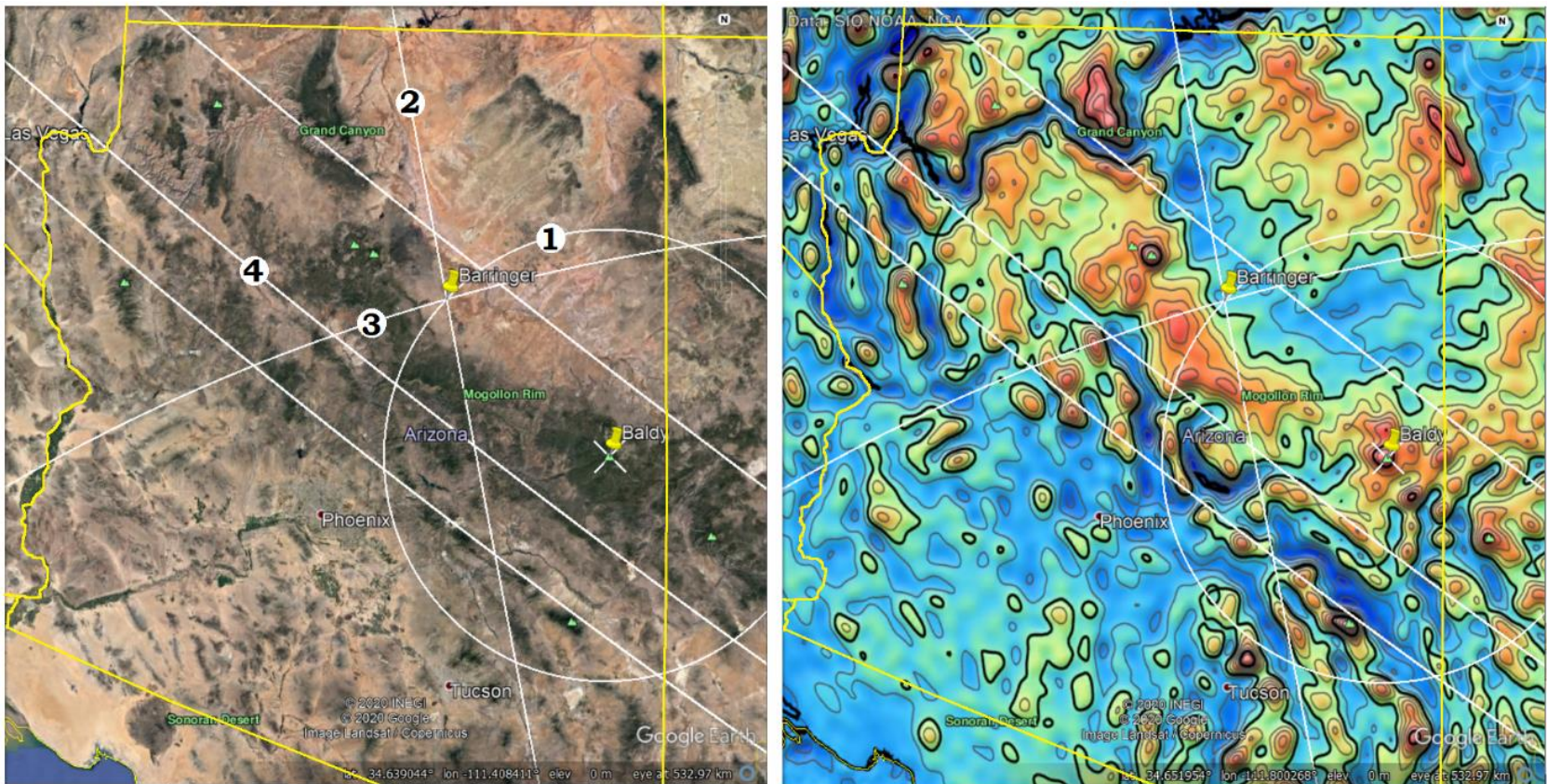

Figure 8.16: (1) CGRS from Baldy crater. (2) CGRS from Verde crater. (3) CGRS from Aguj de Anahuac crater. (4) CGRS from Irminger crater. Left image is Landsat, right image is Global Gravity Anomaly image (Scripps 2014) of same area.

Figure 8.17A shows a whitish cloud of "dust" around the Meteor crater. It gives a strong impression of laying in wind streak, from a southwest wind across the limestone cape of the area. It was identified by Shoemaker (1974) originally as pluvial lake deposits both inside and outside the crater, but there is no evidence of shorelines or other runoff or connected water erosion patterns. More recent studies have classed the high albedo breccia (Figure 8.16) as windblown erosion. Both Ramsey (2002) and Wright and Ramsey (2006) looked at the high albedo area with airborne thermal infrared multispectral scanner and identified the dust as Coconino sandstone and Kaibab limestone. While the Moenkopi siltstone can be differentiated in thermal infrared, it is not visible in the fine breccia.

An alternative interpretation for the fine spotty breccia's location is recognizing in Figure 8.17, CGRS 1. The spotty occurrence of breccia rims many small faults concentric to Baldy stress center. I propose the ejecta did not come out of the crater, but from the many small faults that opened up due to the expanding shock-wave bubble. As the compression wave was propelled down these faults, adiabatic rubble from both the crater and the fault walls was propelled as ejecta up and out, and is now the perceived ejecta. This would account for the spotty nature of the ejecta, and the distribution pattern reflects the direction pressure could travel in the faults. Assuming Baldy crater's faults were the most recent, they would be the easiest to open, but to the northwest some of the Verde faults also opened.

This occurrence of breccia means ejecta was not ballistically ejected from the crater primarily forming the rim, Figure 8.3, but arose from many faults that were forced open by the expanding shock-wave, that also produced the adiabatic rubble. Much of the adiabatic rubble was pushed into the Verde (2) and Aguj de Anahuac (3) faults to form the crater rim and even contributed to the cross ("erosional") ridges that were not primarily erosional at all. This leads to questions concerning the genesis of California's foothills and mountains ridges that show linear trends, Chapters 6-7.
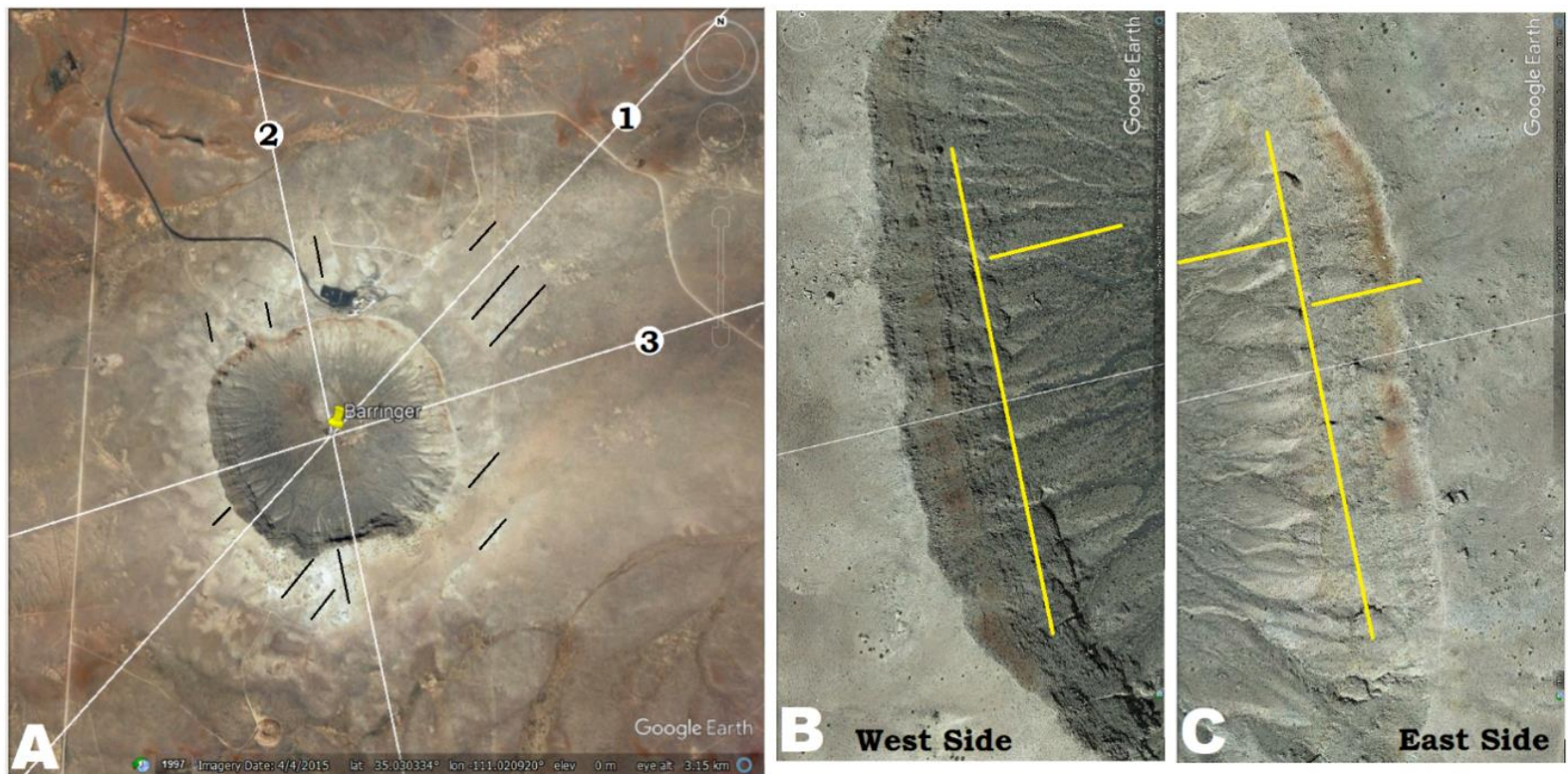
Figure 8.17: (A) Aerial view of Barringer Crater showing white reflection of ejecta dust and small rubble. (B) West and East walls of the crater showing Aguj de Anahuac center's scissor faults.
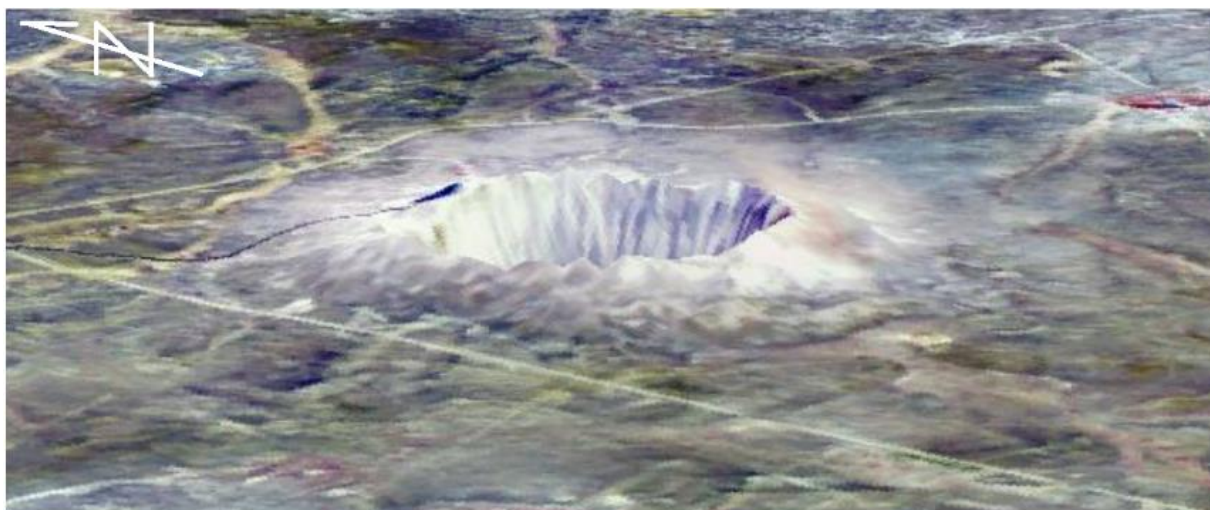

Figure 8.18: ASTER albedo image of Meteor Crater, showing the high albedo ejecta field around the crater. While not detailed, it shows the reality of the color and depth of the crater. (Image credit: NASA.)

Sudbury Crater

Located in Sudbury, Ontario, Sudbury Crater is thought to be one of the oldest impacts craters on earth. Occurring as an elliptical valley (Figure 2B), about 60 km long and 25 km wide; its shape is occasionally associated with an oblique impact, but more regularly with erosion or tectonic forces. It lies on the edge of the Canadian Shield where Plate Tectonics model the shield meeting Grenville Terrane in the Grenville Orogeny with a collision from the east. This collision is cited as the source of the elliptical shape.

Along with abundant shatter cones and shocked quartz in the country rock, nickel and copper deposits are located in the deepest layer above the basement (Wichman93). This mineral association is reminiscent of Saul's (1978) location of mineral mines at junctions of multiple circular lineaments in Arizona and Colorado, where multiple lineaments contributed greater energy

Keweenaw Peninsula and Isle Royal sites in Lake Superior region are significant native copper deposits, and they are both between the circular lineaments from Great Lakes Center, Figure 8.19A. Lineament 1 would be the shock wave (OCR) and lineament 2 would define the inside of the release wave valley, so the metal deposits occur within the release wave valley of this original cratering event.

It is propose the copper, nickel and other metals were brought up by the Great Lakes impactor event. Then the metals were brought up further by the large white circle (3) where it overlapped the Great Lakes crater. The red ring added its lift, and finally the black crater brought it within reach of the surface. The straight linears, CGRS, opened up with the shock-wave of the black crater, like the Baldy

center's ejecta faults of the Meteor crater in Arizona. That would make the concentrations of copper and nickel part of the ejecta that were brought up some more and trapped in the offset dyke system where it is mined today.

The red, purple, and green linears are three sets of CGRS forming the major linear trends used by the dykes. The purple CGRS combined energy with the white circle (3) caused the uplift and northwest thrust that formed the southern ridge of the Sudbury basin valley. This is exactly the movement of the Altai Scarp northwest of the Piccolomini crater in forming the Mare Nectaris' OCR ring (Figure 8.8C). Not only does the occurrence of successive craters in a single area raise the temperature of the rock, but each successive cratering event would lift the valuable minerals ever higher from its original position in the mantle until they reach mining distance of the surface.
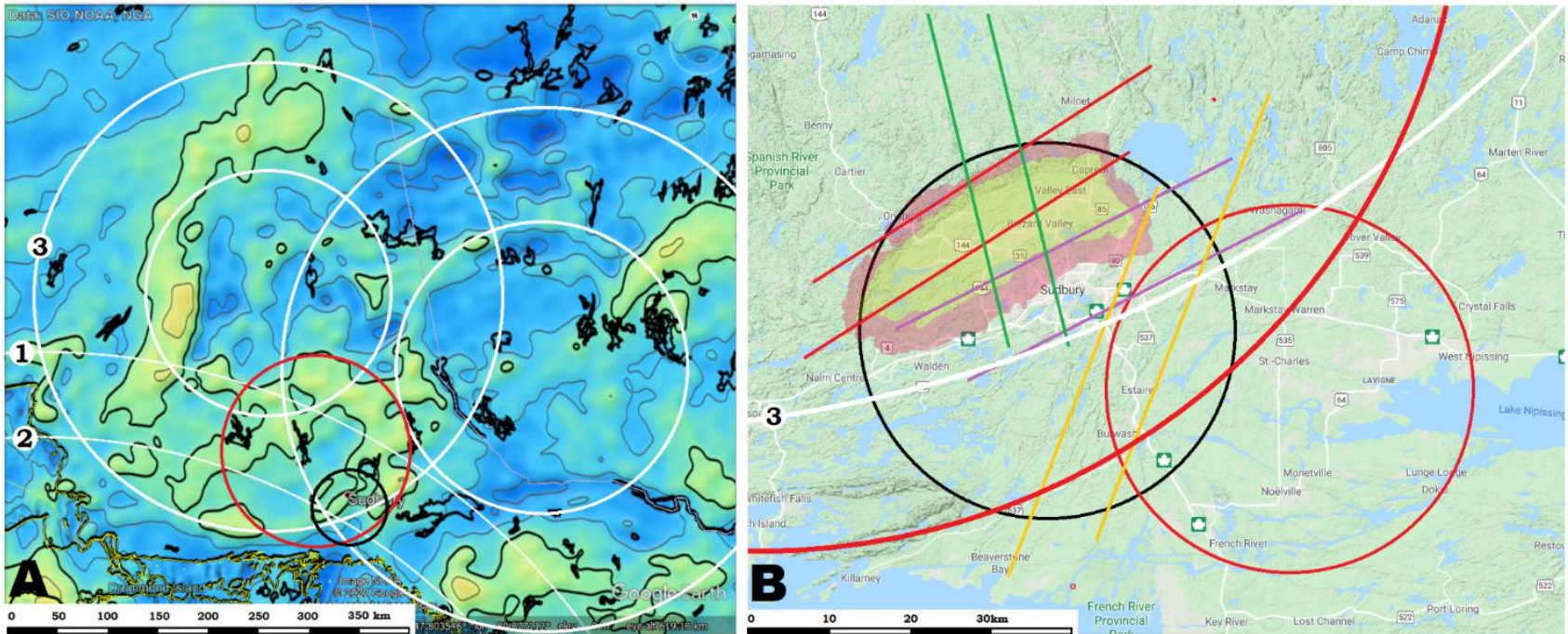

Figure 8.19: (A) Circular lineaments associated with Sudbury Crater. Great Lakes circles, linears 1 and 2, center at 42.36ºN and -85.75ºE, defines the Lower Michigan Basin. Large white western circle centers at 48.45ºN and -81.66ºE. Red circle centers at 46.96ºN and -81.30ºE. Black circle centers at 46.46ºN and -80.97ºE. (B) Black circle is same in both figures. Terrain map from Google Maps showing location of probable crater for Sudbury Structure in black. Additional circle in red and four sets of linears that contributed to shape Sudbury and its minerals.

Vredefort Structure, the ghost crater

Unlike Meteor and Sudbury craters, Vredefort Dome has little visible evidence of a surface crater beyond the center dome of granulite and amphibolite, about 10-12 km radius and the "collar" around the north at 35 km radius. Yet, circular linears extend out past the 230 km radius of its OCR ring (Ring 5, Figure 20). While there is a somewhat bowl shaped set of sediments covering the greater reaches of the Vredefort structure (seen in Figure 8.20D) it is connected with the Koster crater centered just northwest of the center of the Vredefort. Had the sediments originated in the vapor cloud from the Vredefort, it would have covered the crater's center, rather than the granulite and amphibolite that was brought up from under the West Rand Group.

Straight linears from CGRS also play a very significant role in defining the Vredefort structure. Figure 8.20A shows linear 6 defines the east end of the collar, while linear 4 defines the west end of the collar. Different linear trends are visible in each image as different linears are visible at different resolutions.
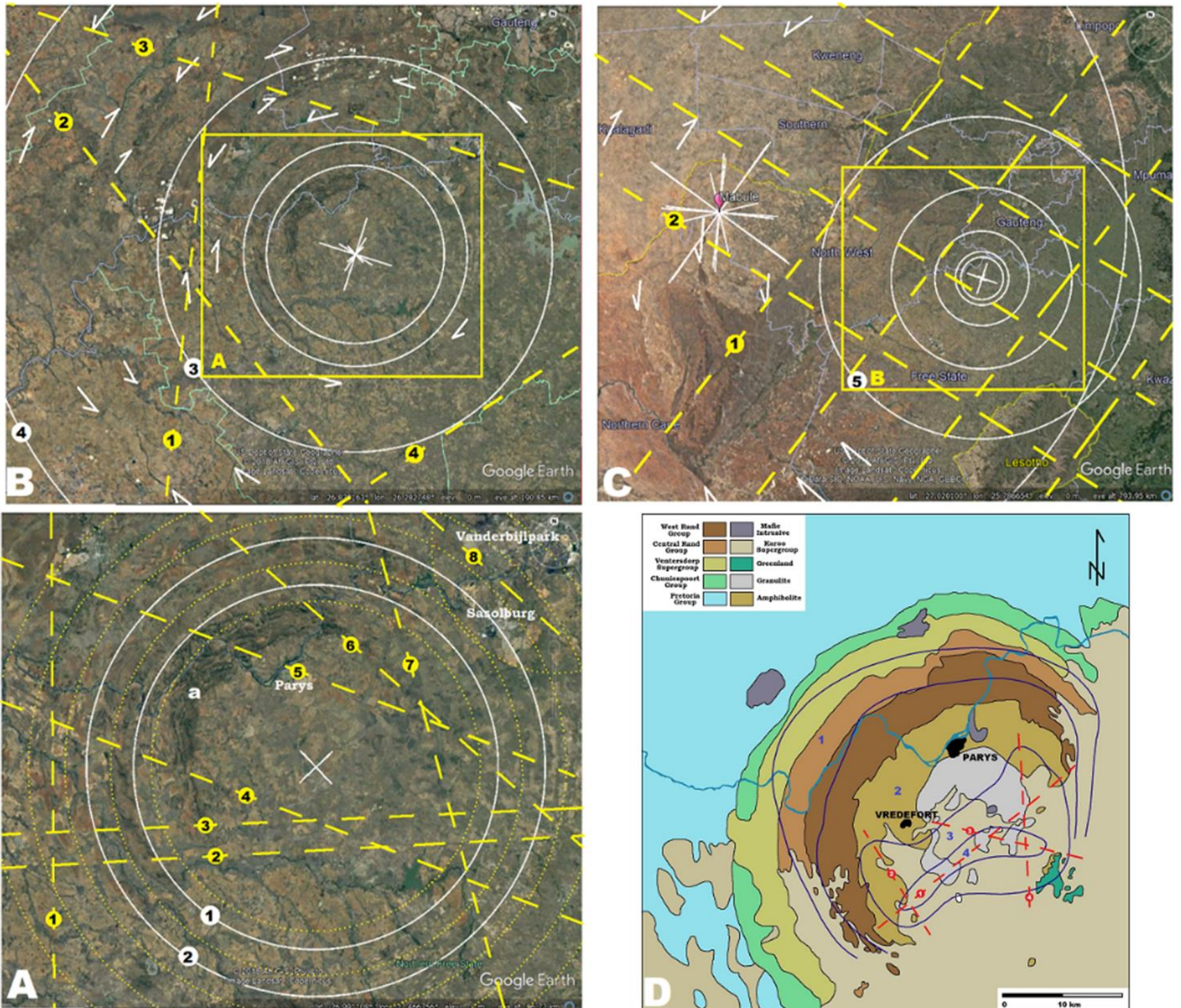
Figure 8.20: The mappable rings of the Vredefort crater, with number 5 just beyond the OCR at ~500 km diameter, and some of the CGRS in the area. Collar (a) is 24 -33 km from center.

While the Vredefort is centered over the famous goldfields of South Africa (Figure 8.21), and the CGRS that the gold fields are located on are evident on the surface around the Vredefort, I do not feel it was in anyway connected to the occurrence of those goldfields, as they were already formed and buried before the Vredefort structure developed.
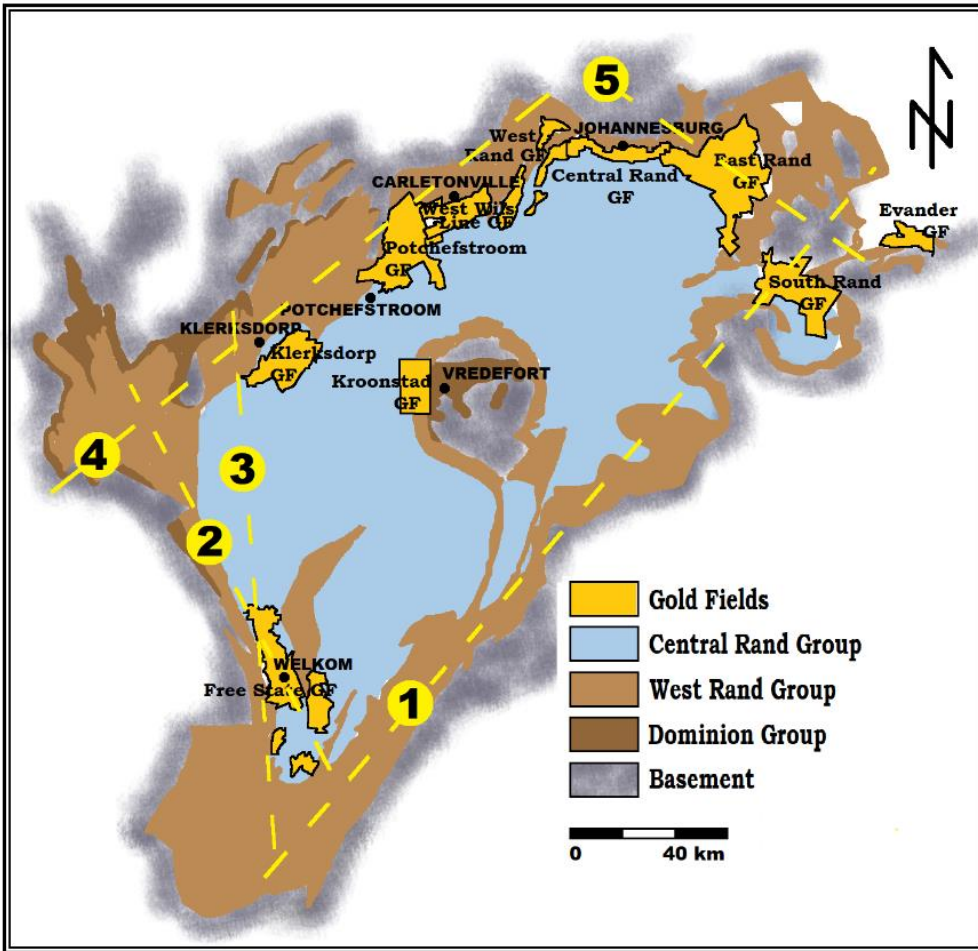
Figure 8.21: The gold fields of South Africa and their spatial relationship to the Vredefort Dome and some of the CGRS in the area. Numbers for linears do not correlate between images.

As a ghost crater, the Vredefort Dome structure does not exist alone, but within a group of large craters (Figure 8.22) including the Mabule, Koster, Giyant, and Indlovu craters and a host of other ghost craters. To understand the sediments of the Witwatersrand and deposition of gold involves all of these craters and several CGRS.
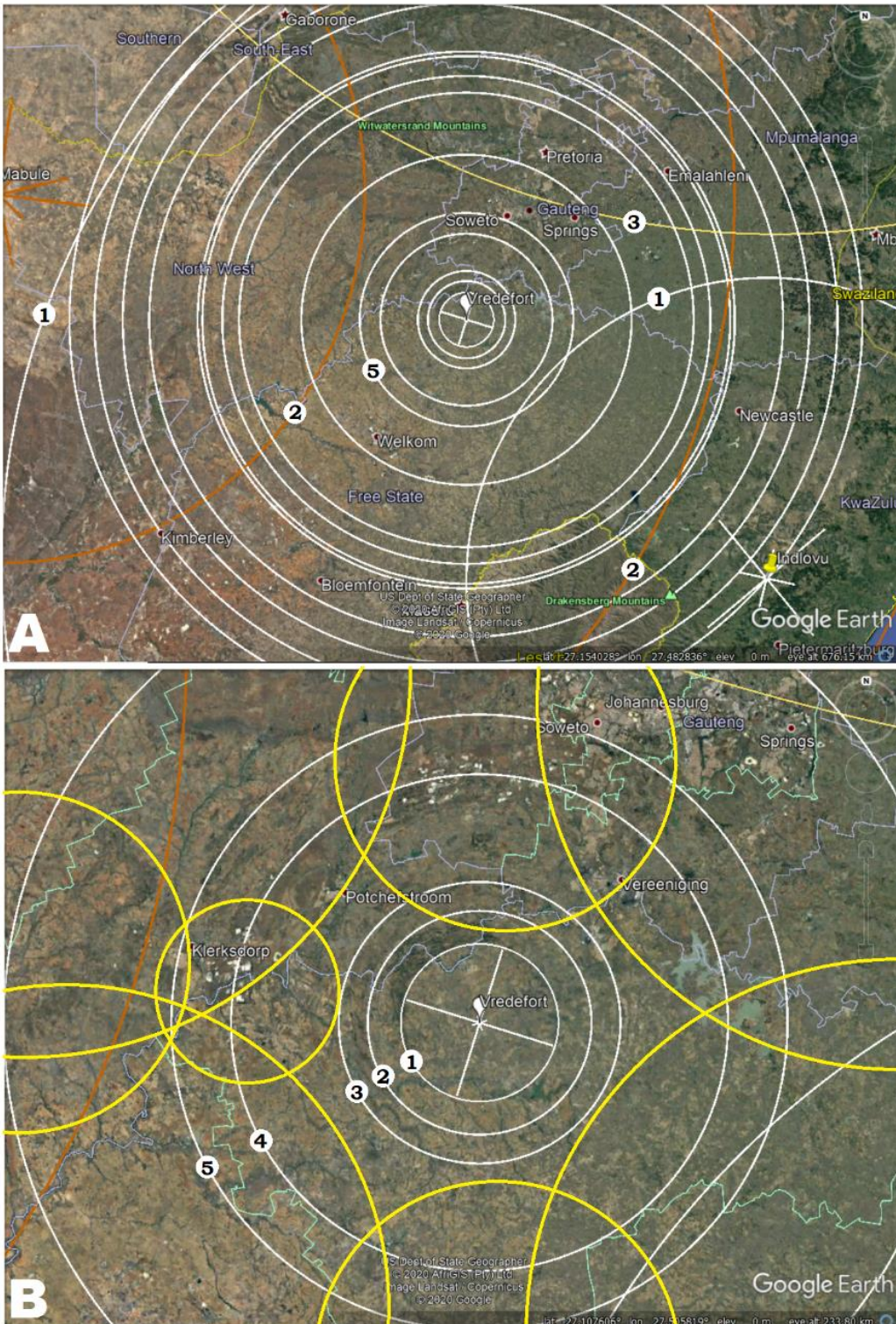
Figure 8.22: (A)(1) Inner and OCR ring for the Indlovu crater, shown in white. (2) Inner and OCR ring for the Mabule crater, shown in red. (B)(1-5) Five rings of the Vredefort Crater. Red ring to west is Mabule inner ring. White ring to southeast is Indlovu inner ring. Yellow rings some of the other ghost craters seen in topography.

Conclusions

There are three conditions found in moon and earth craters that are not commonly recognized: the number of ghost craters adding to the lithology's heat sink, the number and location of CGRSs adding to that heat sink, and the sustained high temperature of the heat sink necessary to accounts for the high percentage of ghost craters and visible CGRSs all formed within the sustained heat prior to the cooling period.

Identification of the ghost craters associated with Mare Nectaris and Mare Orientale suggest the number is 100-1000 times as great as the present count of craters. Given how ghost craters interact with visible craters suggest a short period of interaction time to produce those pattern before significant portions of the latent heat dissipated. While there is no other internal evidence that the cratering period was short, it is consistent with the cratering being a major portion of the events of the Flood year. Having Flood waters cover the impacts in the later Flood's receding stage would more quickly dissipate the heat and temporarily provide a much warmer mean ocean temperature.

References

Chiba, T. 2019. Red relief image map of moon: Asia Air Survey, National Astronomical Observatory of Japan, Geospatial Information Authority of Japan, Japan Aerospace Exploration Agency, https://www.gsi.go.jp/chirijoho/chirijoho41026.html, accessed 9/13/19.

Hartmann, W.K., and G.P. Kuiper. 1962. Concentric Structures surrounding lunar basins, *Communications of the Lunar and Planetary Laboratory* 1(1):51-66.

Mustard, J.F., C.M. Pieters, P.J. Isaacson, J.W. Head, S. Besse, R.N. Clark, R.L. Klima, N.E. Petro, M.I. Staid, J.M. Sunshine, C.J. Runyon, and S. Tompkins. 2011. Compositional diversity and geologic insights of the Aristarchus crater from Moon Mineralogy Mapper data. *Journal of Geophysical Research,* 16(E00G12).

Ramsey, M.S. 2002. Ejecta distribution patterns at Meteor Crater, Arizona: On the applicability of lithologic end-member deconvolution for spaceborne thermal infrared data of Earth and mars, *Journal of Geophysical Research* 107(E8, 5059).

Saul, J.M. 1978. Circular structures of large scale and great age at the Earth's surface. *Nature* 271:345-349.

Scripps Institute of Oceanography. 2014. Global [Marine] Gravity Anomaly download. http://topex.ucsd.edu/grav_outreach/, accessed 11/19/2014.

Shoemaker, E.M. 1974. Barringer Meteorite Crater, Coconino County, Arizona. In *Guidebook to the Geology of Barringer Meteorite Crater, Arizona*. Shoemaker, E.M. and S.W. Kieffer (editors) Publication no. 17, Reprinted 1988, Center for Meteorite Studies, Arizona State University, Tempe, Arizona: 1-11.

Wright, S. P., and M. S. Ramsey. 2006. Thermal infrared data analyses of Meteor Crater, Arizona: Implications for Mars spaceborne data from the Thermal Emission Imaging System, *Journal of Geophysical Research* 111 (E02004).